International Journal of Heat and Fluid Flow 31 (2010) 217–226

Contents lists available at ScienceDirect

International Journal of Heat and Fluid Flow

journal homepage: www.elsevier.com/locate/ijhff

Numerical investigation of double-diffusive (natural) convection in vertical annuluses with opposing temperature and concentration gradients

Sheng Chen [a,b], Jonas Tölke [b], Manfred Krafczyk [b,*]

[a] State Key Lab of Coal Combustion, Huazhong University of Science and Technology, Wuhan 430074, China
[b] Institute for Computational Modeling in Civil Engineering, Technical University, Braunschweig 38106, Germany

ARTICLE INFO

Article history:
Received 8 April 2009
Received in revised form 21 December 2009
Accepted 26 December 2009
Available online 8 February 2010

Keywords:
Lattice Boltzmann model
Double-diffusive convection

ABSTRACT

Double-diffusive convection in vertical annuluses with opposing temperature and concentration gradients is of fundamental interest and practical importance. However, available literature especially for higher Rayleigh numbers beyond $Ra \leqslant 10^5$ is sparse. In this study, we investigated double diffusion induced convection up to $Ra = 10^7$ using a simple lattice Boltzmann model. Thanks to the good stability of the present model, a modest grid resolution is sufficient for the present simulations. The influences of the ratio of buoyancy forces $0.8 \leqslant N \leqslant 1.3$, the aspect ratio $0.5 \leqslant A \leqslant 2$ and the radius ratio $1.5 \leqslant K \leqslant 3$ on heat and mass transfer characteristics are discussed in detail.

1. Introduction

Double-diffusive convection, i.e. flows generated by buoyancy due to simultaneous temperature and concentration gradients are ubiquitous in natural as well as technical systems. In nature such flows are frequently encountered in oceans, lakes, solar pounds, shallow coastal waters and the atmosphere. In industry examples include chemical processes, crystal growth, energy storage, material processing such as solidification, food processing etc. For a review of the fundamental work in this area, see Turner (1974) and Schmitt (1994).

Available studies related to double-diffusive convection are mostly concerned with rectangular cavities. Pioneering experiments were carried out by Kamotani et al. (1985). Their work showed that when a stable stratified solution is heated from one side, multicellular flow structures can be observed. Later, Gobin and Bennacer (1996) identified the different regimes dominated by thermal or solutal effects in terms of the buoyancy ratio and the Lewis number based on numerical simulations. The instability of double-diffusive convection has been studied analytically by Bardan et al. (2000). More recently, Sezai and Mohamad (2000) and Bergeon and Knobloch (2002) carried out three-dimensional numerical simulations on double-diffusive convection in cubic cavities, to cite only a few. However, there are only few studies on double-diffusive convection in vertical annuluses (Retiel et al., 2006), although convection related phenomena in vertical annuluses are scientifically more interesting than those in rectangular/cubic cavities (Turner, 1974). Shipp et al. (1993), Shipp et al. (1993) investigated thermosolutal convection in concentric annular cavities at low and moderate Lewis numbers. Bennacer et al. (2000) simulated the thermosolutal convection in vertical annular cavities containing a porous medium. Recently Retiel et al. (2006) investigated the effect of the curvature ratio on convectional patterns. The latest work on double-diffusive convection in vertical annuluses was conducted by Bennacer et al. (2009). In their work, they studied the Soret effect for double-diffusive convection in detail. In almost all previous works on this field, the Rayleigh number was relatively low ($Ra \leqslant 10^5$).

In the present work, the double-diffusive convection in vertical annuluses with opposing temperature and concentration gradients is reported for higher Rayleigh numbers up to $Ra = 10^7$. The influences of the ratio of buoyancy forces $0.8 \leqslant N \leqslant 1.3$, the aspect ratio $0.5 \leqslant A \leqslant 2$ and the radius ratio $1.5 \leqslant K \leqslant 3$ on heat and mass transfer characteristics are discussed in detail in this study. In order to numerically solve the governing equations for such double-diffusive convection, a simple lattice Boltzmann (LB) model, which is an extension of the model proposed in our previous works (Chen et al., 2008; Chen et al., 2009), is employed in this paper. The present model possesses three obvious advantages inherited from our previous models (Chen et al., 2008; Chen and Tolke, 2009):

1. The present model is algorithmically simple, which is an attractive advantage for both practitioners and novices.
2. Tts stability and low numerical viscosity allows the use of relatively coarse grids for flow with high Rayleigh numbers which reduces computational costs. and

* Corresponding author.
E-mail addresses: shengchen.hust@gmail.com (S. Chen), kraft@irmb.tu-bs.de (M. Krafczyk).

0142-727X/$ - see front matter © 2010 Elsevier Inc. All rights reserved.
doi:10.1016/j.ijheatfluidflow.2009.12.013

Nomenclature

c	fluid particle speed
Ω_k	collision term in Eq. (31)
D	coefficient related to Eq. (31)
$\vec{u}$	fluid velocity vector
$\vec{e}_k$	discrete velocity
$\Upsilon_{o,k}, \Omega'_k$	source terms in Eqs. (25), (31)
$\vec{g}$	gravity
g_k, f_k	distribution function for Eqs. (17), (18) and Eq. (19)
g_k^{eq}, f_k^{eq}	equilibrium distribution function for Eqs. (1)–(3)
H	height of simulation domain
S	Svanberg vorticity
T	temperature
R	radius
N	ratio of buoyancy forces
Pr	Prandtl number
Le	Lewis number
Ra	Rayleigh number
p	pressure
K	curvature ratio
A	aspect ratio
$\vec{x}$	phase space

Greek symbols

Δx, Δt	grid spacing, time step
κ	thermal conductivity
α	expansion coefficient
ν	kinematic viscosity
ω, ψ	vorticity, streamfunction
τ	relaxation time for Eq. (25)
τ_ψ	relaxation time for Eq. (31)
ρ	density
ζ	dimensionless time
ζ_k, ξ_k	weights for equilibrium distribution function
δ, χ	coefficients in Eqs. (29) and (30)
μ	dynamic viscosity

Subscripts and superscripts

μ	dynamic viscosity
o, i	outer, inner
0	reference value
k	discrete velocity direction
c	concentration
T	temperature

3. The derivation of the present model is quite straightforward as is often observed for kinetic models (see also the recent review Yu et al., 2003).

2. Governing equations for double-diffusive convection in vertical annuluses

The configuration of the vertical annulus is illustrated in Fig. 1. The inner wall with the radius R_i and the outer wall with R_o. $K = R_o/R_i$ is the radius ratio. The aspect ratio is defined as $A = H/(R_o - R_i)$, where H is the height of the annular cavity.

Based on the Boussinesq assumption, the primitive-variables-based governing equations for double-diffusive convection in the cylindrical coordinate system can be written as (Retiel et al., 2006; Shipp et al., 1993; Shipp et al., 1993; Chamkha and Al-Naser, 2002)

$$\frac{1}{r}\frac{\partial(ru)}{\partial r} + \frac{\partial w}{\partial z} = 0, \tag{1}$$

$$\frac{\partial u}{\partial t} + u\frac{\partial u}{\partial r} + w\frac{\partial u}{\partial z} = -\frac{1}{\rho}\frac{\partial p}{\partial r} + \nu\nabla^2 u, \tag{2}$$

$$\frac{\partial w}{\partial t} + u\frac{\partial w}{\partial r} + w\frac{\partial w}{\partial z} = -\frac{1}{\rho}\frac{\partial p}{\partial z} + \nu\nabla^2 w + g\alpha_T(T - T_0) - g\alpha_c(C - C_0), \tag{3}$$

$$\frac{\partial T}{\partial t} + u\frac{\partial T}{\partial r} + w\frac{\partial T}{\partial z} = \kappa\nabla^2 T, \tag{4}$$

$$\frac{\partial C}{\partial t} + u\frac{\partial C}{\partial r} + w\frac{\partial C}{\partial z} = D\nabla^2 C, \tag{5}$$

where

$$\nabla^2 = \frac{1}{r}\frac{\partial}{\partial r}\left(r\frac{\partial}{\partial r}\right) + \frac{\partial^2}{\partial z^2}.$$

u and it w are radial and axial velocity components, p is the pressure, T is the temperature, C is the concentration, ν is the kinematic viscosity, g is the gravitational acceleration along the negative z-axis, κ is the thermal conductivity, ρ is the density, D is the species diffusivity, α_T and α_c represent the coefficients of thermal expansion and compositional expansion respectively.

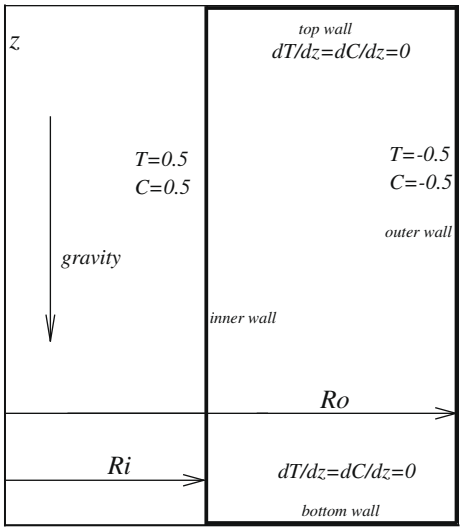

Fig. 1. Configuration of the computational domain and boundary conditions.

For double-diffusive convection in a cylindrical coordinate system, computation time can be reduced if the problem is reformulated so that the three variables u, w, p are eliminated in favor of the vorticity ω and the Stokes streamfunction ψ (Chen et al., 2008; Chamkha and Al-Naser, 2002; Langlois, 1985; Chen et al., 2008), which are defined as

$$\omega = \frac{\partial w}{\partial r} - \frac{\partial u}{\partial z}, \tag{6}$$

$$u = \frac{1}{r}\frac{\partial \psi}{\partial z}, \tag{7}$$

$$w = -\frac{1}{r}\frac{\partial \psi}{\partial r}. \tag{8}$$

The dimensionless vorticity–streamfunction-based governing equations read (Retiel et al., 2006; Shipp et al., 1993; Shipp et al., 1993)

$$\frac{\partial \widetilde{S}}{\partial \widetilde{t}}+\widetilde{u}\frac{\partial \widetilde{S}}{\partial \widetilde{r}}+\widetilde{w}\frac{\partial \widetilde{S}}{\partial \widetilde{z}} = \frac{Pr}{\widetilde{r}}\left(\frac{\partial \widetilde{T}}{\partial \widetilde{r}}-N\frac{\partial \widetilde{C}}{\partial \widetilde{r}}\right)+\frac{Pr}{Ra^{1/2}}\left\{\frac{1}{\widetilde{r}}\frac{\partial}{\partial \widetilde{r}}\left[\frac{1}{\widetilde{r}}\frac{\partial}{\partial \widetilde{r}}(\widetilde{r}^2\widetilde{S})\right]+\frac{\partial^2 \widetilde{S}}{\partial \widetilde{z}^2}\right\}, \tag{9}$$

$$\frac{\partial \widetilde{T}}{\partial \widetilde{t}}+\widetilde{u}\frac{\partial \widetilde{T}}{\partial \widetilde{r}}+w\frac{\partial \widetilde{T}}{\partial \widetilde{z}}=\frac{1}{Ra^{1/2}}\left[\frac{1}{\widetilde{r}}\frac{\partial}{\partial \widetilde{r}}\left(\widetilde{r}\frac{\partial \widetilde{T}}{\partial \widetilde{r}}\right)+\frac{\partial^2 \widetilde{T}}{\partial \widetilde{z}^2}\right], \tag{10}$$

$$\frac{\partial \widetilde{C}}{\partial \widetilde{t}}+\widetilde{u}\frac{\partial \widetilde{C}}{\partial \widetilde{r}}+w\frac{\partial \widetilde{C}}{\partial \widetilde{z}}=\frac{1}{LeRa^{1/2}}\left[\frac{1}{\widetilde{r}}\frac{\partial}{\partial \widetilde{r}}\left(\widetilde{r}\frac{\partial \widetilde{C}}{\partial \widetilde{r}}\right)+\frac{\partial^2 \widetilde{C}}{\partial \widetilde{z}^2}\right],, \tag{11}$$

$$\frac{\partial}{\partial \widetilde{r}}\left(\frac{1}{\widetilde{r}}\frac{\partial \widetilde{\psi}}{\partial \widetilde{r}}\right)+\frac{1}{\widetilde{r}}\frac{\partial^2 \widetilde{\psi}}{\partial \widetilde{z}^2}=-\widetilde{r}\widetilde{S}. \tag{12}$$

in the above equations the parameters with tildes represent the dimensionless counterparts. We omit the tildes from this point on for clarity. $S=\omega/r$ is the Svanberg vorticity (Langlois, 1985). $Pr=\nu/\kappa$ is the Prandtl number, $Le=\kappa/D$ is the Lewis number and $Ra=g\alpha_T(T-T_0)(R_o-R_i)^3/\nu\kappa$ the thermal Rayleigh number. $N=\alpha_c(C-C_0)/\alpha_T(T-T_0)$ is the ratio of buoyancy forces.

In the present study, the boundary conditions are: $\psi=u=w=0$ at all walls, $T=0.5$ and $C=0.5$ at the inner wall, $T=-0.5$ and $C=-0.5$ at the outer wall and $\partial T/\partial z=\partial C/\partial z=0$ at the top and bottom walls. The initial conditions are $\psi=u=w=0$, $T=-0.5$ and $C=-0.5$. The value of Svanberg vorticity S at walls is calculated using the method proposed in Ref. (Chen et al., 2008).

3. A lattice Boltzmann model for double-diffusive convection in vertical annuluses

By performing the following coordinate transformation (Chen et al., 2008; Peng et al., 2003; Halliday et al., 2001; Reis and Phillips, 2008):

$$(r,z)\mapsto(x,y), \tag{13}$$

$$(u,w)\mapsto(u,v). \tag{14}$$

Eqs. (7)–(12) can be written in pseudo-cartesian coordinates:

$$u=\frac{1}{x}\frac{\partial \psi}{\partial y}, \tag{15}$$

$$v=-\frac{1}{x}\frac{\partial \psi}{\partial x}, \tag{16}$$

$$\frac{\partial S}{\partial t}+u\frac{\partial S}{\partial x}+v\frac{\partial S}{\partial y}=\frac{Pr}{Ra^{1/2}}\left(\frac{\partial^2 S}{\partial x^2}+\frac{\partial^2 S}{\partial y^2}\right)+S_o, \tag{17}$$

$$\frac{\partial T}{\partial t}+u\frac{\partial T}{\partial x}+v\frac{\partial T}{\partial y}=\frac{1}{Ra^{1/2}}\left(\frac{\partial^2 T}{\partial x^2}+\frac{\partial^2 T}{\partial y^2}\right)+T_o, \tag{18}$$

$$\frac{\partial C}{\partial t}+u\frac{\partial C}{\partial x}+v\frac{\partial C}{\partial y}=\frac{1}{LeRa^{1/2}}\left(\frac{\partial^2 C}{\partial x^2}+\frac{\partial^2 C}{\partial y^2}\right)+C_o, \tag{19}$$

$$\frac{\partial^2 \psi}{\partial y^2}+\frac{\partial^2 \psi}{\partial x^2}=\Theta. \tag{20}$$

In Eqs. (17)–(20), the source terms caused by the coordinate transformation and the buoyant forcing due to the temperature and concentration read

$$S_o=\frac{3}{x}\frac{Pr}{Ra^{1/2}}\frac{\partial S}{\partial x}+\frac{Pr}{x}\left(\frac{\partial T}{\partial x}-N\frac{\partial C}{\partial x}\right), \tag{21}$$

$$T_o=\frac{1}{Ra^{1/2}}\frac{1}{x}\frac{\partial T}{\partial x}, \tag{22}$$

$$C_o=\frac{1}{LeRa^{1/2}}\frac{1}{x}\frac{\partial C}{\partial x}, \tag{23}$$

$$\Theta=-(x^2S+v). \tag{24}$$

We note that subsequently u and v stand for the velocity components along x- and y-coordinates.

Eq. (17) (governing equation for the flow field), Eq. (18) (governing equation for the temperature field) and Eq. (19) (governing equation for the concentration field) have the same advection–diffusion form (including source terms), but with different coefficients. There are many matured efficient lattice Boltzmann models for this type of equation (Chen et al., 2008). In this paper a D2Q5 model is employed to solve these equations which reads:

$$g_k(\vec{x}+c\vec{e}_k\Delta t,t+\Delta t)-g_k(\vec{x},t) = -\tau^{-1}[g_k(\vec{x},t)-g_k^{(eq)}(\vec{x},t)]+\Delta t\Upsilon_{o,k}, \tag{25}$$

where $\vec{e}_k$ $(k=0,\ldots,4)$ are the discrete velocity directions:

$$\vec{e}_k=\begin{cases}(0,0) & k=0,\\ (\cos(k-1)\pi/2,\ \sin(k-1)\pi/2) & k=1,2,3,4.\end{cases}$$

$c=\Delta x/\Delta t$ is the fluid particle speed. Δx, Δt and τ are the lattice grid spacing, the time step and the dimensionless relaxation time respectively. $\Upsilon_{o,k}$ is the discrete form of the source term Υ_o (Chen et al., 2008; Chen et al., 2007), $\Upsilon_o=S_o,\ T_o,\ C_o$ for Eqs. (17)–(19), respectively. $\Upsilon_{o,k}$ satisfies:

$$\sum_{k\geqslant 0}\Upsilon_{o,k}=\Upsilon_o. \tag{26}$$

The simplest choice satisfying the constraint Eq. (26) is

$$\Upsilon_{o,k}=\frac{\Upsilon_o}{5} \tag{27}$$

The equilibrium distribution $g_k^{(eq)}$ is defined by

$$g_k^{(eq)}=\frac{\delta}{5}\left[1+2.5\frac{\vec{e}_k\cdot\vec{u}}{c}\right], \tag{28}$$

$\delta=S,T,C$ for Eqs. (17)–(19), respectively and is obtained by

$$\delta=\sum_{k\geqslant 0}g_k, \tag{29}$$

and the dimensionless relaxation time τ is determined by

$$\chi=\frac{2c^2(\tau-0.5)}{5}, \tag{30}$$

$\chi=\frac{Pr}{Ra^{1/2}},\frac{1}{Ra^{1/2}},\frac{1}{LeRa^{1/2}}$ for Eqs. (17)–(19), respectively.

Eq. (20) is just the Poisson equation, which also can be solved by the LB method (Mei et al., 2006). In the present study, the D2Q5 model used in our previous work (Chen et al., 2008; Chen et al., 2008) is employed. The evolution equation for Eq. (20) reads

$$f_k(\vec{x}+c\vec{e}_k\Delta t,t+\Delta t)-f_k(\vec{x},t)=\Omega_k+\Omega_k', \tag{31}$$

where $\Omega_k=-\tau_\psi^{-1}[f_k(\vec{x},t)-f_k^{(eq)}(\vec{x},t)]$, $\Omega_k'=\Delta t\zeta_k\Theta D$ and $D=\frac{c^2}{2}(0.5-\tau_\psi)$. $\tau_\psi>0.5$ is the dimensionless relaxation time (Chen et al., 2008). $f_k^{(eq)}$ is the equilibrium distribution function, and defined by

$$f_k^{(eq)}=\begin{cases}(\xi_0-1.0)\psi: & k=0,\\ \xi_k\psi: & k=1,2,3,4.\end{cases}$$

ξ_k and ζ_k are weight parameters given as $\xi_0=\zeta_0=0$, $\xi_k=\zeta_k=1/4(k=1,\ldots,4)$. ψ is obtained by

$$\psi=\sum_{k\geqslant 1}f_k. \tag{32}$$

The detailed derivation from Eqs. (25) and (31) to Eqs. (17)–(20) can be found in our previous work (Chen et al., 2009).

4. Numerical validation

Firstly we validated the present model by setting $K = 1.0$ and $A = 2.0$ which means the infinite curvature and represents a rectangular cavity (Retiel et al., 2006). A grid resolution 100×200 is used for the simulation. Figs. 2 and 3 illustrate the isothermal lines, the isoconcentration lines and the stream lines for $N = 0.8$ and $N = 1.3$ respectively, with $Pr = 1.0$, $Le = 2.0$, $Ra = 10^5$. For simplicity, the abscissa is normalized by $(r - R_i)/(R_o - R_i)$, and the ordinate is normalized by $z/(R_o - R_i)$ for all figures in this paper. When $N < 1.0$, the flow is primarily dominated by thermal buoyancy effects, and a large central clockwise thermal recirculation is predicted with horizontally non-uniform isotherms in the core region within the enclosure. Furthermore, the concentration contours are distorted in the core of the enclosure with a stable stratification in the vertical direction except near the insulated walls of the enclosure. A stagnant zone in the corners of the enclosure is also observed. In contrast, for $N > 1.0$ the flow is mainly dominated by compositional buoyancy effects. For $N = 1.3$, a counterclockwise compositional recirculation exists in the core region of the enclosure along with two clockwise thermal recirculations occurring near the top right and bottom left corners of the enclosure. The contours for temperature and concentration are almost parallel to each other within the center of the enclosure away from the walls. In both cases, the isothermal lines, the isoconcentration lines and the stream lines are all point symmetric with respect to the geometric center of the enclosure. The results obtained by the present model agree well with those in Ref. (Chamkha and Al-Naser, 2002).

To further quantify the results, the average Nusselt number Nu and the average Sherwood number Sh at the inner wall obtained by the present model are listed in Table 1 together with reference values from Ref. (Chamkha and Al-Naser, 2002). The average Nusselt number Nu is calculated by

$$\mathrm{Nu} = -\int_0^H \left(\frac{\partial T}{\partial r}\right) dz, \tag{33}$$

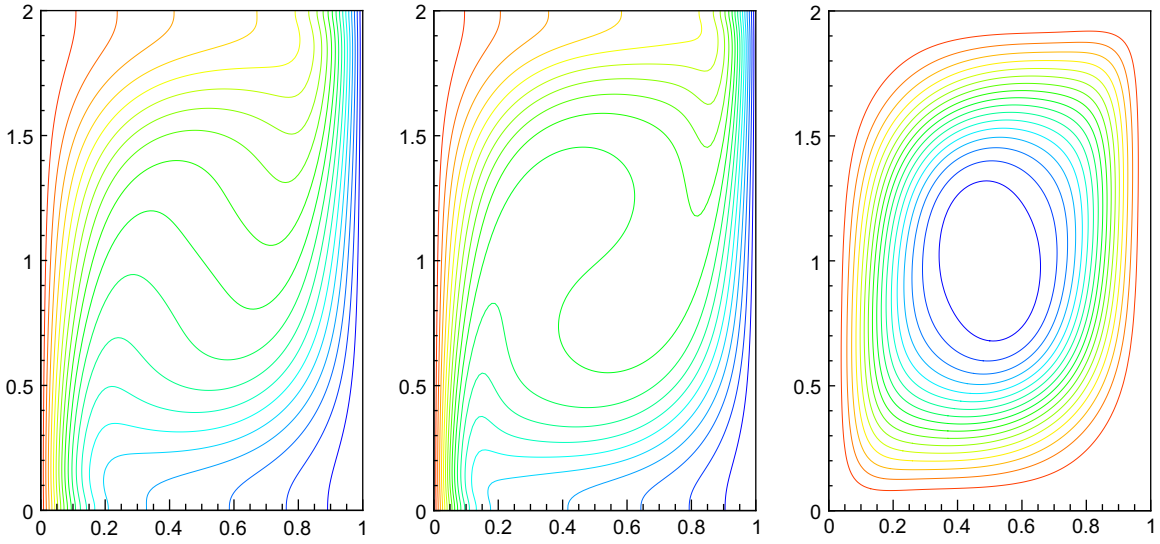

Fig. 2. Isothermal lines, isoconcentration lines and stream lines for $Pr = 1.0$, $Le = 2.0$, $Ra = 10^5$, $N = 0.8$, $A = 2.0$ and $K = 1.0$.

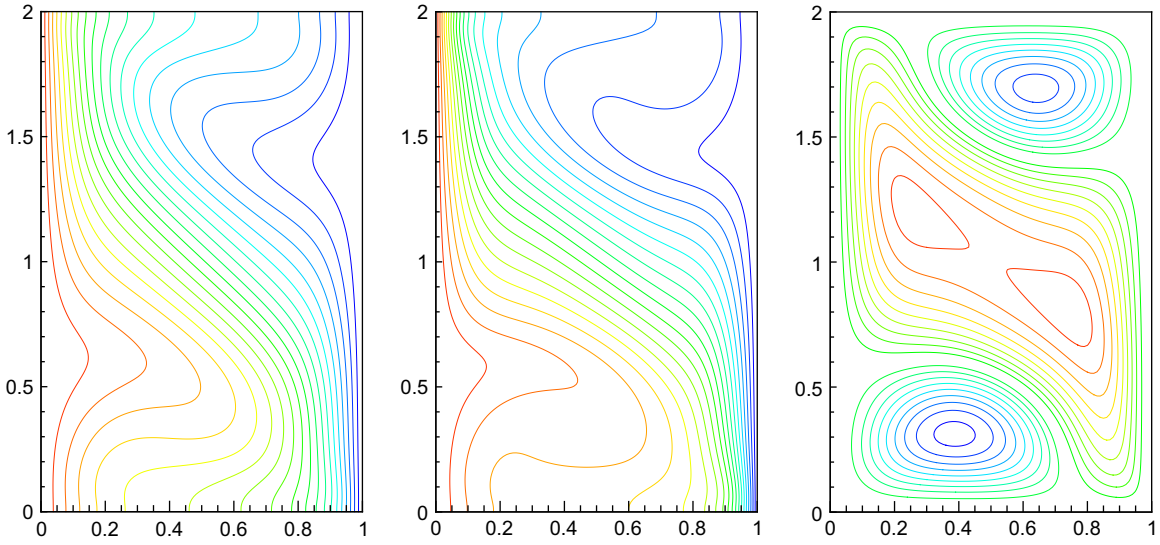

Fig. 3. Isothermal lines, isoconcentration lines and stream lines for $Pr = 1.0$, $Le = 2.0$, $Ra = 10^5$, $N = 1.3$, $A = 2.0$ and $K = 1.0$.

Table 1
Average Nusselt number *Nu* and average Sherwood number *Sh*.

	Nu		*Sh*	
	Ref. Chamkha and Al-Naser (2002)	Present	Ref. Chamkha and Al-Naser (2002)	Present
$N = 0.8$	3.67	3.6897	4.89	4.9156
$N = 1.3$	2.10	2.1255	3.15	3.1615

and the average Sherwood number Sh is calculated by

$$\mathrm{Sh} = -\int_{0^H} \left(\frac{\partial C}{\partial r}\right) dz. \tag{34}$$

Figs. 4 and 5 illustrate the comparison of local values for velocity, isoconcentrations and isotherms obtained by the present model with those obtained by the finite difference scheme (Chamkha and Al-Naser, 2002). The good agreement between them demonstrates the capability of the present model again.

It is well known that the stability of a numerical scheme may vary with respect to boundary conditions and other parameters. In order to give the reader an impression of the stability limit for the present schme the numerical experiments presented below indicated that the minimum non-dimensional relaxation time of the present model is about 0.503 which allows simulations with element Raleigh numbers up to $Ra_{\Delta x} \simeq \mathcal{O}(10^5)$.

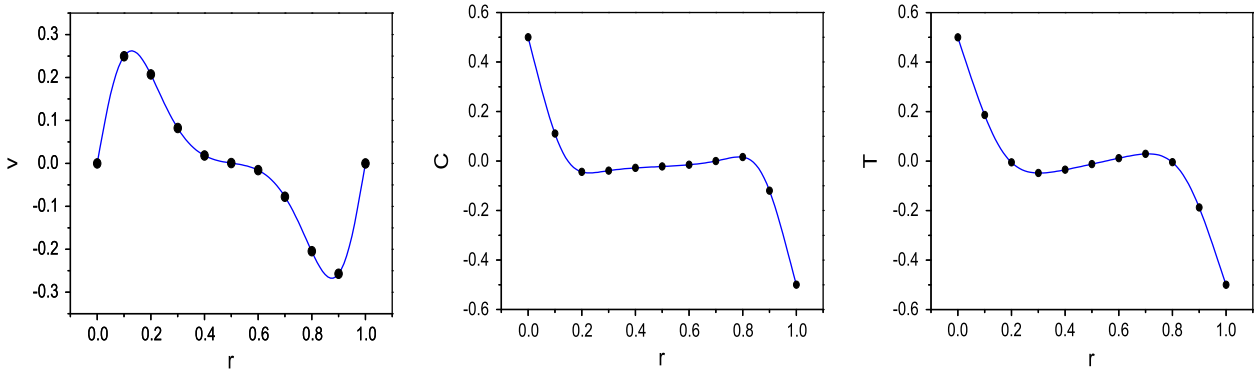

Fig. 4. Comparison of velocity, isoconcentrations and isotherms for $Pr = 1.0$, $Le = 2.0$, $Ra = 10^5$, $N = 0.8$, $A = 2.0$ and $K = 1.0$ along the line $Z = 1.0$: dot-Ref. (Chamkha and Al-Naser, 2002); line-present results.

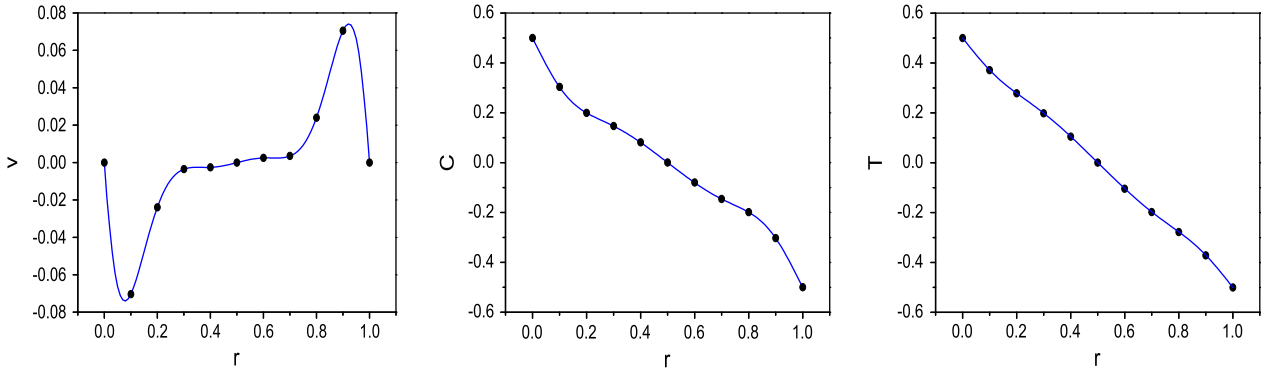

Fig. 5. Comparison of velocity, isoconcentrations and isotherms for $Pr = 1.0$, $Le = 2.0$, $Ra = 10^5$, $N = 1.3$, $A = 2.0$ and $K = 1.0$ along the line $Z = 1.0$: dot-Ref. (Chamkha and Al-Naser, 2002); line-present results.

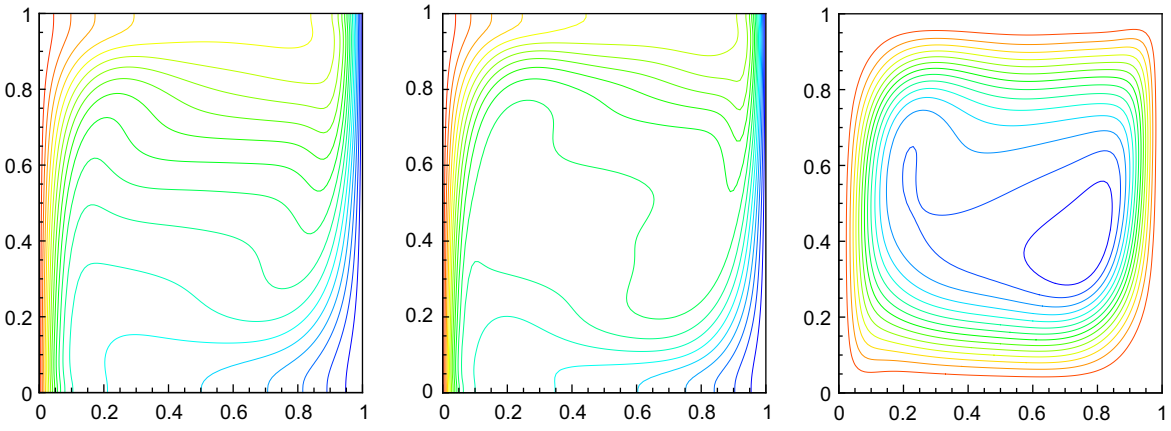

Fig. 6. Isothermal lines, isoconcentration lines and stream lines for $Pr = 1.0$, $Le = 2.0$, $Ra = 10^6$, $N = 0.8$, $A = 1.0$ and $K = 1.5$.

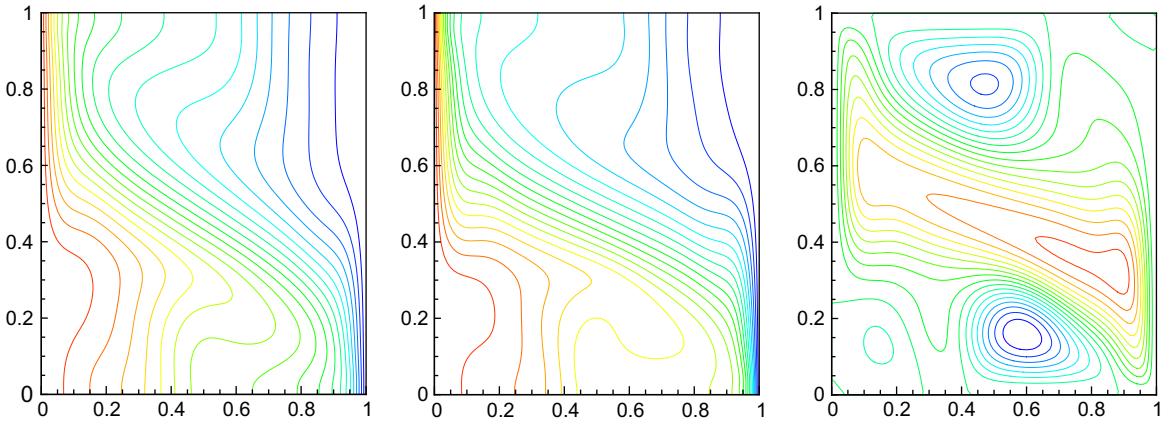

Fig. 7. Isothermal lines, isoconcentration lines and stream lines for $Pr = 1.0$, $Le = 2.0$, $Ra = 10^6$, $N = 1.3$, $A = 1.0$ and $K = 1.5$.

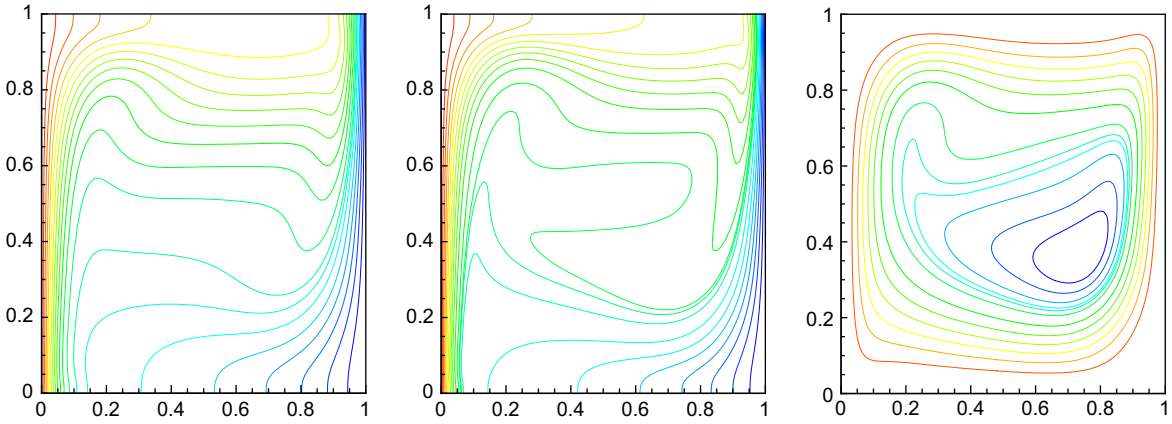

Fig. 8. Isothermal lines, isoconcentration lines and stream lines for $Pr = 1.0$, $Le = 2.0$, $Ra = 10^6$, $N = 0.8$, $A = 1.0$ and $K = 2.0$.

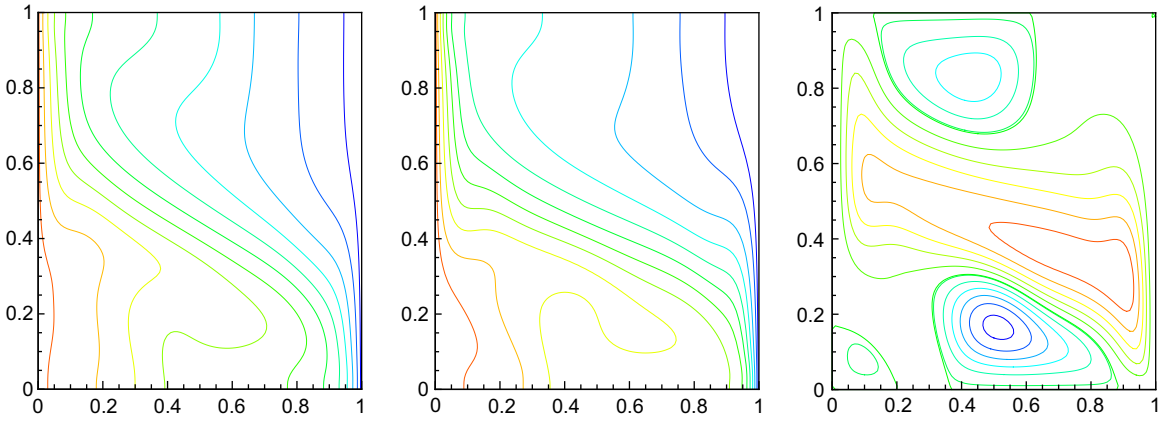

Fig. 9. Isothermal lines, isoconcentration lines and stream lines for $Pr = 1.0$, $Le = 2.0$, $Ra = 10^6$, $N = 1.3$, $A = 1.0$ and $K = 2.0$.

5. Results and discussion

In the present study, we investigated double-diffusive convection in vertical annuluses with opposing temperature and concentration gradients with $Ra = 10^6$, 10^7. To the best of our knowledge, available publications discussing double-diffusive convection in vertical annuluses are limited to a range of $Ra \leqslant 10^5$ (Retiel et al., 2006; Shipp et al., 1993; Shipp et al., 1993), and there are few studies on higher *Ra*.

The other parameters in the simulation are: $Pr = 1.0$, $Le = 2.0$, $0.8 \leqslant N \leqslant 1.3$, $0.5 \leqslant A \leqslant 2$ and $1.5 \leqslant K \leqslant 3.0$. The grid resolution is fixed to 100 for the horizontal direction and varies from 50 to 200 for the vertical direction according to different values for *A*. Figs. 6–15 show the numerical results for $Ra = 10^6$.

For $K \neq 1.0$, the isothermal lines, the isoconcentration lines and the stream lines are no longer point symmetric. While $N < 1.0$, the flow is primarily dominated by thermal buoyancy effects and one large clockwise thermal recirculation appears with horizontally

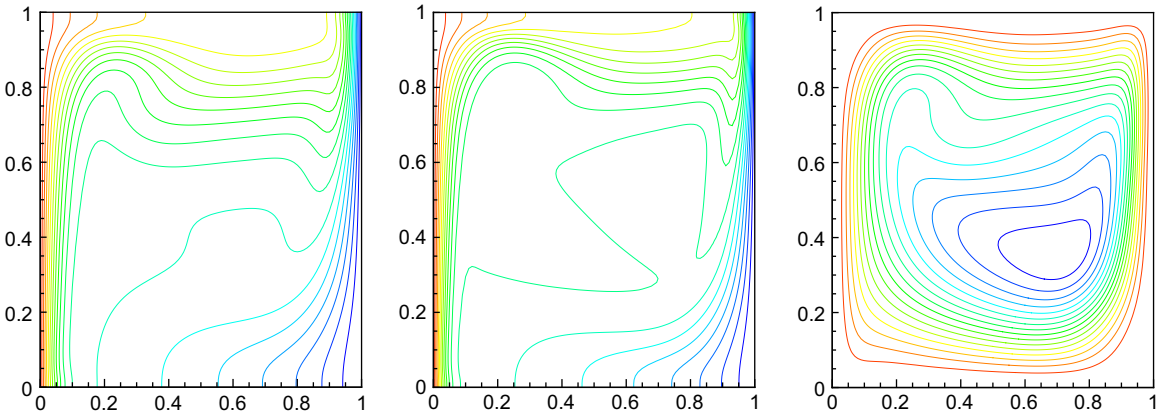

Fig. 10. Isothermal lines, isoconcentration lines and stream lines for $Pr = 1.0$, $Le = 2.0$, $Ra = 10^6$, $N = 0.8$, $A = 1.0$ and $K = 3.0$.

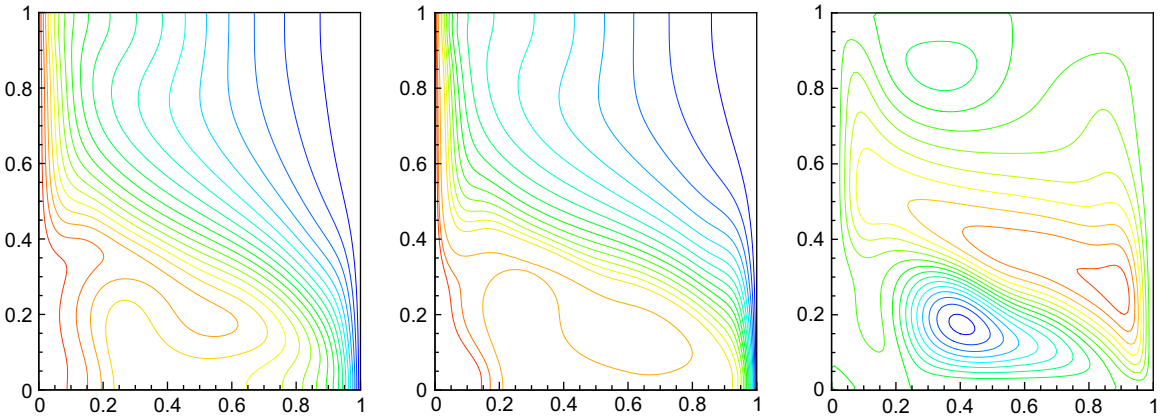

Fig. 11. Isothermal lines, isoconcentration lines and stream lines for $Pr = 1.0$, $Le = 2.0$, $Ra = 10^6$, $N = 1.3$, $A = 1.0$ and $K = 3.0$.

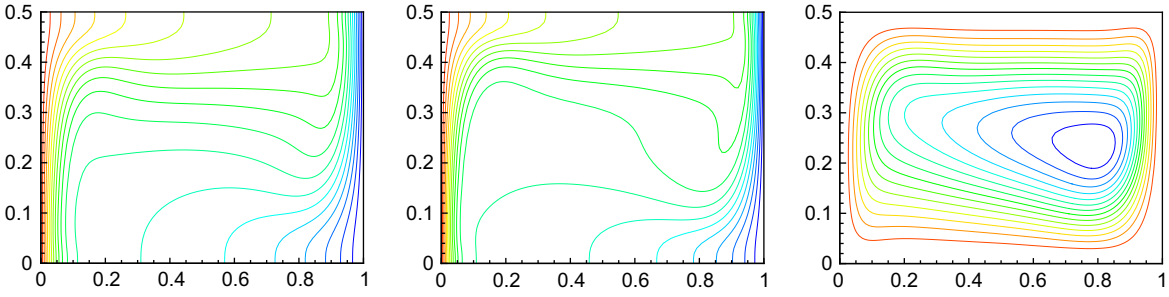

Fig. 12. Isothermal lines, isoconcentration lines and stream lines for $Pr = 1.0$, $Le = 2.0$, $Ra = 10^6$, $N = 0.8$, $A = 0.5$ and $K = 2.0$.

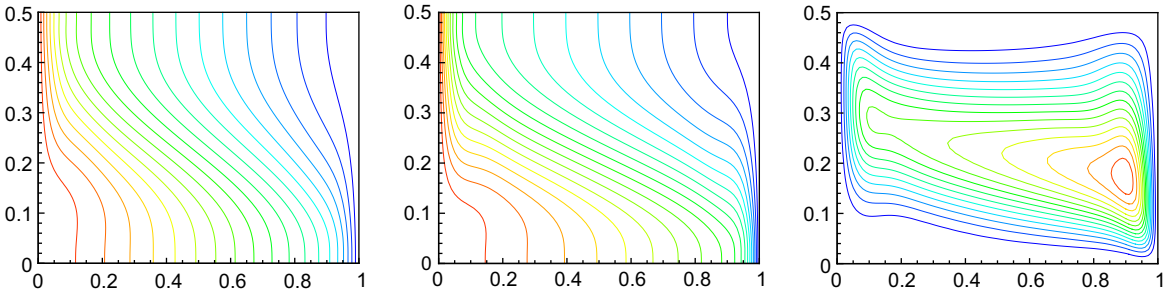

Fig. 13. Isothermal lines, isoconcentration lines and stream lines for $Pr = 1.0$, $Le = 2.0$, $Ra = 10^6$, $N = 1.3$, $A = 0.5$ and $K = 2.0$.

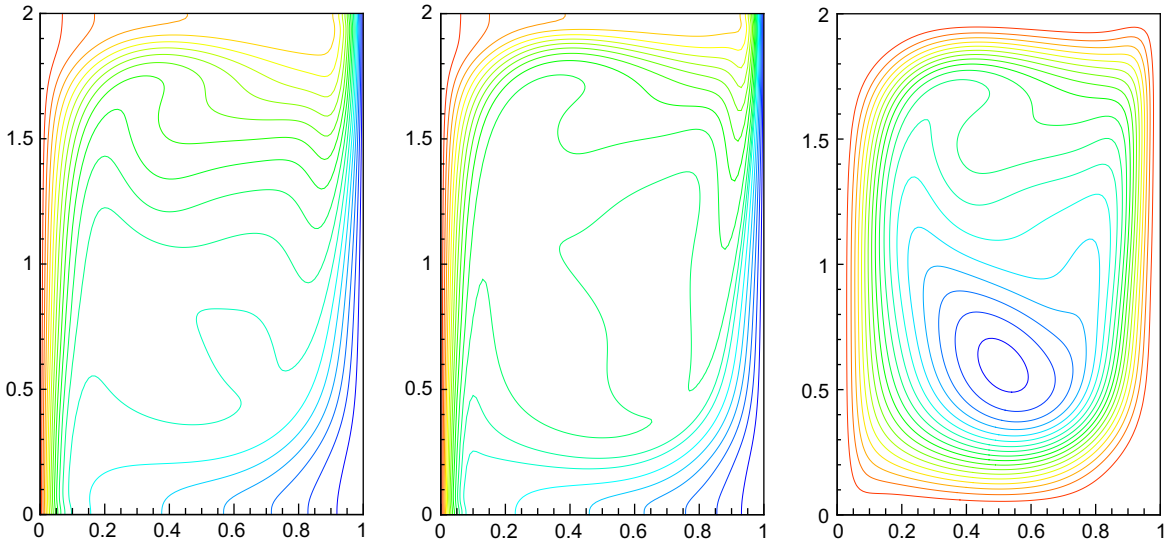

Fig. 14. Isothermal lines, isoconcentration lines and stream lines for $Pr = 1.0$, $Le = 2.0$, $Ra = 10^6$, $N = 0.8$, $A = 2.0$ and $K = 2.0$.

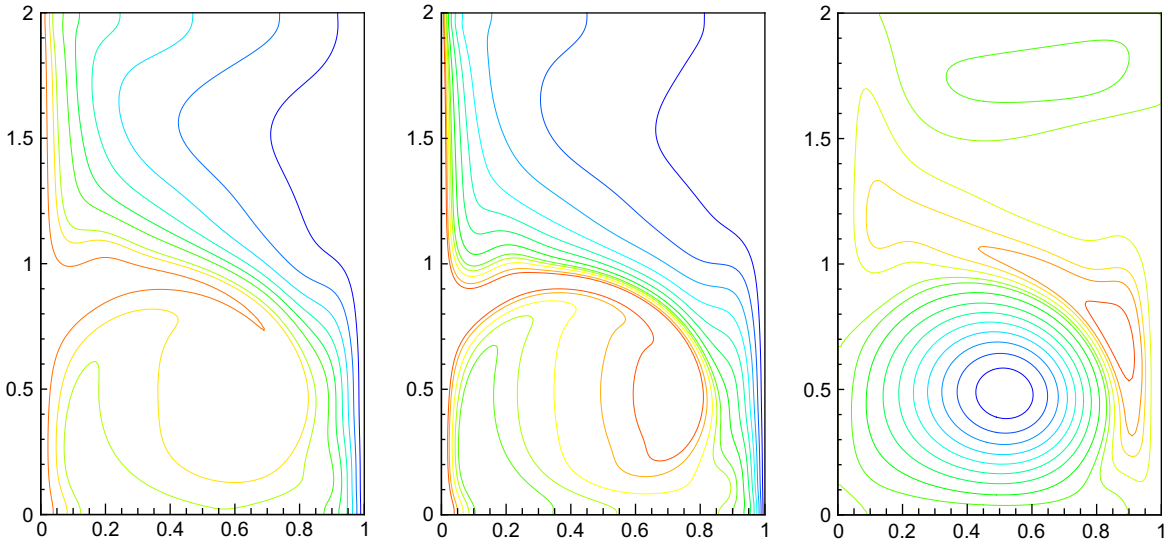

Fig. 15. Isothermal lines, isoconcentration lines and stream lines for $Pr = 1.0$, $Le = 2.0$, $Ra = 10^6$, $N = 1.3$, $A = 2.0$ and $K = 2.0$.

non-uniform isotherms in the core region within the enclosure. The vortex center is located close to the outer wall and below the center of the enclosure. As K increases, the cylinders drift apart and the gradients at the inner wall are lower than that at the outer one . In addition, the vortex center is slightly shifted downwards. For low values of K, the concentration contours are distorted only in the core of the enclosure with a stable stratification in the vertical direction except near the insulated walls of the enclosure. With increasing K, the distorted region expands to the bottom of the enclosure. The influence of K on the isothermal lines and the isoconcentration lines at the top is smaller than at the bottom. In the shallow enclosure $(A = 0.5)$, the vortex center is closer to the outer wall and the horizontal midplane of the enclosure. The concentration and temperature contours are less disturbed by the absence of symmetry than the for the counterpart with $A = 1.0$. However, for the tall enclosure $A = 2.0$, the level of distortion of the isothermal and the isoconcentration lines is more significant than for lower values of A. The vortex center moves more closely to the vertical midplane of the enclosure and further away from the horizontal midplane. When $N > 1.0$ the flow is mainly dominated by compositional buoyancy effects, whereas for $N < 1.0$ the number of vortices varies depending on K and A. For the shallow enclosure $A = 0.5$ and $K = 2.0$, there is only one counterclockwise compositional recirculation. For constant $KA = 1.0$, we observe a counterclockwise compositional recirculation in the core region of the enclosure together with three clockwise thermal recirculations occurring near the top and bottom corners of the enclosure, among them one near the top and two in the vicinity of the bottom. If A increases, there is still one counterclockwise compositional recirculation along with three clockwise thermal recirculations, although the clockwise thermal recirculation which is closest to the bottom left corner becomes very small. On the contrary, the other two clockwise thermal recirculations expand obviously. Especially, the clockwise thermal recirculation farther away from the bottom left corner almost occupies half of the cross section. The counterclockwise compositional recirculation is compressed into a very narrow region by the clockwise thermal recirculations. These changes are also reflected by the isothermal

Table 2
Average Nusselt number *Nu*.

	$N = 0.8$	$N = 1.3$
$A = 1.0,\ K = 1.5$	6.6045	2.9163
$A = 1.0,\ K = 2.0$	6.8463	3.0187
$A = 1.0,\ K = 3.0$	7.0163	3.3631
$A = 0.5,\ K = 2.0$	6.5778	2.5972
$A = 2.0,\ K = 2.0$	6.3335	3.9056

Table 3
Average Sherwood number *Sh*.

	$N = 0.8$	$N = 1.3$
$A = 1.0,\ K = 1.5$	8.3451	5.0899
$A = 1.0,\ K = 2.0$	8.7006	5.2019
$A = 1.0,\ K = 3.0$	8.8462	5.5581
$A = 0.5,\ K = 2.0$	8.5514	5.0826
$A = 2.0,\ K = 2.0$	8.0023	5.7536

and isoconcentration lines. For $A = 0.5$, the isothermal and isoconcentration lines are nearly point symmetric except at the bottom left and the top right corners. Temperature and concentration contours are almost parallel to each other within the center of the enclosure away from the walls. As A increases, the isothermal and isoconcentration lines are distorted obviously and are no longer parallel, especially in the low half part of the enclosure and the plumes starting from the inner wall move farther, almost reaching the outer wall. It is obvious that in tall enclosures ($N > 1.0$), thermal buoyancy effects play an increasingly important role in the lower half part of the annulus as A increases. When $K = 1.5$ and $A = 1.0$, there is one counterclockwise compositional recirculation

Table 4
Average Nusselt number *Nu* and Sherwood number *Sh* for $Ra = 10^7$.

	Nu	*Sh*
$N = 0.8$	12.3830	16.5019
$N = 1.3$	6.9965	10.8668

in the core region of the enclosure together with five perceptible clockwise thermal recirculations occurring near the top and bottom corners of the enclosure. With increasing K, the counterclockwise compositional recirculation and one of the clockwise thermal recirculations obviously expand, but the others are significantly compressed. For $K = 3.0$, there are only three clockwise thermal recirculations remaining whereas for $K = 1.5$ contours for temperature and concentration are almost parallel to each other within the center of the enclosure away from the walls and are distorted as K increases. The plumes starting from the inner wall can approach the outer wall more easily with bigger K.

Tables 2 and 3 list the average Nusselt number *Nu* and the average Sherwood number *Sh* at the inner wall obtained by the present model. It is clear that *Nu* and *Sh* both are monotonic increasing functions of K within the range of parameters of the present study. *Nu* and *Sh* also both are monotonic increasing functions of A when $N = 1.3$ but not for $N = 0.8$. These conclusions are in agreement with previous literature discussing low *Ra* results (Retiel et al., 2006; Chamkha and Al-Naser, 2002).

Figs. 16, 17 illustrate the numerical results for $Ra = 10^7$, $A = 1.0$ and $K = 2.0$ with grid resolution 200×200. Beyond $Ra = 10^7$, we found that the flow field becomes unsteady. The isotherms and isoconcentrations are distorted significantly over the whole domain except near the vertical walls and additional small structures are

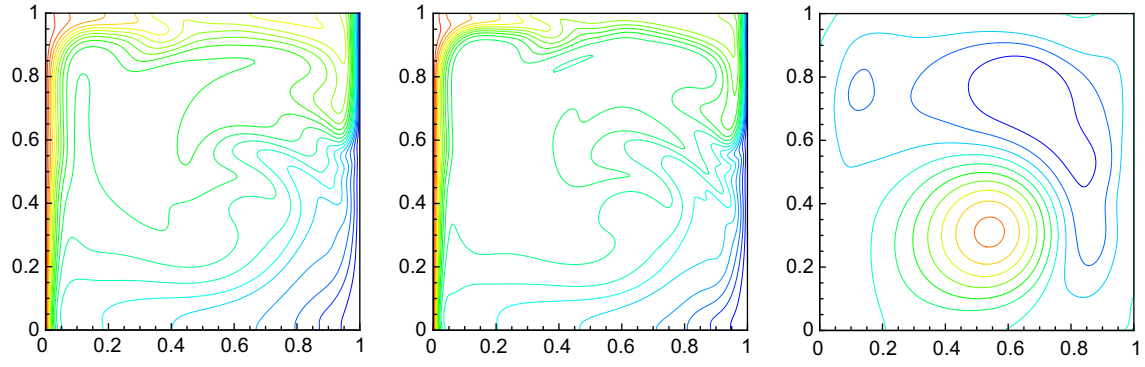

Fig. 16. Isothermal lines, isoconcentration lines and stream lines for $Pr = 1.0$, $Le = 2.0$, $Ra = 10^7$, $N = 0.8$, $A = 1.0$ and $K = 2.0$.

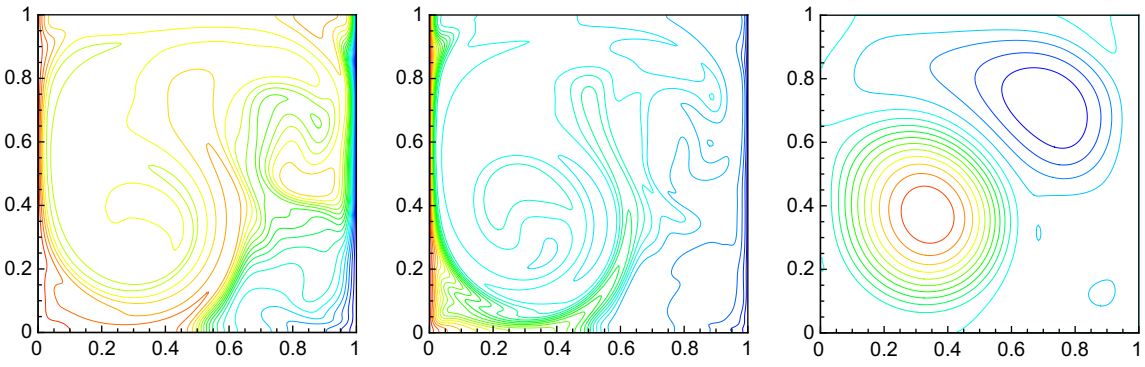

Fig. 17. Isothermal lines, isoconcentration lines and stream lines for $Pr = 1.0$, $Le = 2.0$, $Ra = 10^7$, $N = 1.3$, $A = 1.0$ and $K = 2.0$.

emerging. Table 4 lists the corresponding average Nusselt number *Nu* and Sherwood number *Sh*. It is obvious that *Nu* and *Sh* increase significantly with *Ra*.

6. Conclusion

Double-diffusive convection in vertical annuluses with opposing temperature and concentration gradients is an important issue in basic theory as well as in engineering. Yet, previous related studies are limited to $Ra \leqslant 10^5$.

In the present study, we introduced a simple lattice Boltzmann model to investigate such convectional phenomena at higher Rayleigh number up to $Ra = 10^7$ with $Pr = 1.0$, $Le = 2.0$, $0.8 \leqslant N \leqslant 1.3$, $0.5 \leqslant A \leqslant 2$ and $1.5 \leqslant K \leqslant 3.0$.

Firstly, we validated the present model by setting $K = 1.0$ which represents a rectangular cavity. The results obtained by the present model agree quantitatively well with the data available in the literature. Then we investigated the influences of the ratio of buoyancy forces *N*, the aspect ratio *A* and the radius ratio *K* on the convectional patterns. When $N < 1.0$, the flow is primarily dominated by thermal buoyancy effects, whereas for $N > 1.0$ the flow is mainly dominated by compositional buoyancy effects. For convective flows with $Ra = 10^6$ and $N < 1.0$, there is only one large clockwise thermal recirculation in the enclosure, independent of *K* and *A*. On the contrary, the number of vortices varies depending on *K* and *A* when $N > 1.0$. The average Nusselt number *Nu* and the average Sherwood number *Sh* at the inner wall both are monotonic increasing functions of *K* within the range of parameters of the present study. They are also both monotonic increasing functions of *A* for $N > 1.0$. For Raleigh numbers beyond $Ra = 10^7$, the flow became unsteady which was outside the scope of this work, but which could be readily studied by the present model.

Acknowledgments

This work was partially supported by the Alexander von Humboldt Foundation, Germany.

References

Bardan, G., Bergeon, A., Knobloch, E., Mojtabi, A., 2000. Nonlinear doubly diffusive convection in vertical enclosures. Physica D 138, 91–113.

Bennacer, R., Beji, H., Duval, R., Vasseur, P., 2000. The Brinkman model for thermosolutal convection in a vertical annular porous layer. Int. Commun. Heat Mass Transfer 27, 69–80.

Bennacer, R., Mohamad, A.A., El Ganaoui, M., 2009. Thermodiffusion in porous media: multi-domain constitutant separation. Int. J. Heat Mass Transfer 52, 1725–1733.

Bergeon, A., Knobloch, E., 2002. Natural doubly diffusive convection in three-dimensional enclosures. Phys. Fluids 14, 3233–3250.

Chamkha, A.J., Al-Naser, H., 2002. Hydromagnetic double-diffusive convection in a rectangular enclosure with opposing temperature and concentration gradients. Int. J. Heat Mass Transfer 45, 2465–2483.

Chen, S., Tolke, J., 2009. Numerical simulation of fluid flow and heat transfer inside a rotating disk–cylinder configuration by a lattice Boltzmann model. Phys. Rev. E 80, 016702.

Chen, S., Liu, Z., Zhang, C., et al., 2007. Appl. Math. Comput. 193, 266–284.

Chen, S., Tolke, J., Geller, S., Krafczyk, M., 2008. Lattice Boltzmann model for incompressible axisymmetric flows. Phys. Rev. E 78, 046703.

Chen, S., Tolke, J., Krafczyk, M., 2008. A new method for the numerical solution of vorticity–streamfunction formulations. Comput. Methods Appl. Mech. Eng. 198, 367–376.

Chen, S., Tolke, J., Krafczyk, M., 2009. Simulation of buoyancy-driven flows in a vertical cylinder using a simple lattice Boltzmann model. Phys. Rev. E 79, 016704.

Gobin, D., Bennacer, R., 1996. Cooperation thermosolutal convection in enclosures-II. Heat transfer and flow structure. Int. J. Heat Mass Transfer 39, 2683–2697.

Halliday, I., Hammond, L.A., Care, C.M., Good, K., Stevens, A., 2001. Lattice Boltzmann equation hydrodynamics. Phys. Rev. E 64, 011208/1–011208/8.

Kamotani, Y., Wang, L.W., Ostrach, S., Jiang, H.D., 1985. Experimental study of natural convection in shallow enclosures with horizontal temperature and concentration gradients. Int. J. Heat Mass Transfer 28, 165–173.

Langlois, W.E., 1985. Buoyancy-driven flows in crystal-growth melts. Annu. Rev. Fluid Mech. 17, 191–215.

Mei, R., Luo, L., Lallemand, P., d'Humieres, D., 2006. Consistent initial conditions for lattice Boltzmann simulations. Comput. Fluids 35, 855–862.

Peng, Y., Shu, C., Chew, Y.T., Qiu, J., 2003. Numerical investigation of flows in Czochralski crystal growth by an axisymmetric lattice Boltzmann method. J. Comput. Phys. 186, 295–307.

Reis, T., Phillips, T.N., 2008. Numerical validation of a consistent axisymmetric lattice Boltzmann model. Phys. Rev. E 77, 026703/1–026703/6.

Retiel, N., Bouguerra, E., Aichouni, M., 2006. Effect of curvature ratio on cooperating double-diffusive convection in vertical annular cavities. J. Appli. Sci. 6, 2541–2548.

Schmitt, R.W., 1994. Double diffusion in oceanography. Annu. Rev. Fluid Mech. 26, 255–285.

Sezai, I., Mohamad, A.A., 2000. Double diffusive convection in a cubic enclosure with opposing temperature and concentration gradients. Phys. Fluids 12, 2210–2223.

Shipp, P.W., Shoukri, M., Carver, M.B., 1993. Double diffusive natural convection in a closed annulus. Numer. Heat Transfer, Part A 24, 339–356.

Shipp, P.W., Shoukri, M., Carver, M.B., 1993. Effect of thermal Rayleigh and Lewis numbers on double diffusive natural convection in closed annulus. Numer. Heat Transfer, Part A 24, 451–465.

Turner, J.S., 1974. Double diffusive phenomena. Annu. Rev. Fluid Mech. 6, 37–56.

Yu, D., Mei, R., Luo, L.S., et al., 2003. Viscous flow computations with the method of lattice Boltzmann equation. Prog. Aerospace Sci. 39, 329–367.